metals

MDPI

Article

Effect of Solution Treatment on Microstructure and Corrosion Resistance Performance of HIPed Net-Shaped Duplex Stainless Steel SAF2507

Bingwei Wang [1], Jiahao Liu [1], Zhanfang Wu [2], Pengjie Zhang [2], Lida Che [2] and Dianchun Ju [1,*]

[1] School of Metallurgy Engineering, Jiangsu University of Science and Technology, Zhangjiagang 215600, China
[2] CISRI HIPEX Technology Co., Ltd., Haidian, Beijing 100081, China
* Correspondence: judianchun@just.edu.cn

Abstract

This study systematically investigates the effect of solution treatment on the microstructure and corrosion resistance of duplex stainless steel SAF2507 fabricated by direct hot isostatic pressing (HIP). The HIP specimens were solution treated at 1080 °C for 1 h, followed by comprehensive characterization using SEM, EDS, EBSD, XRD, XPS, and electrochemical testing in 3.5 wt% NaCl solution. Results indicate that solution treatment effectively dissolved intermetallic precipitates, promoted a more uniform distribution of ferrite and austenite phases, and reduced microstructural heterogeneity. Electrochemical impedance spectroscopy and potentiodynamic polarization tests showed that the treated samples exhibited a wider passive region and higher charge transfer resistance, indicating enhanced passivation behavior. XPS analysis further revealed an increased proportion of Cr_2O_3 and O^{2-} and decreased Fe_{hy}^{3+} and H_2O content in the passive film, suggesting improved compactness and chemical stability. Surface morphology analysis confirmed a significant reduction in pitting corrosion after treatment. These findings demonstrate that solution treatment is an effective post-processing method to enhance the corrosion resistance of HIP-fabricated SAF2507 duplex stainless steel.

Keywords: duplex stainless steel; hot isostatic pressing; solution treatment; microstructure evolution; corrosion resistance

1. Introduction

Duplex stainless steels (DSSs), especially super duplex grades such as SAF2507, are widely employed in marine, petrochemical, and offshore industries due to their excellent combination of high mechanical strength and superior corrosion resistance, particularly in chloride-containing environments [1–3]. SAF2507, characterized by a balanced dual-phase microstructure consisting of approximately equal volumes of austenite and ferrite, offers remarkable resistance to localized corrosion, including pitting and crevice corrosion, as well as stress corrosion cracking [4–6].

In recent years, hot isostatic pressing (HIP) has received considerable attention as an advanced manufacturing technique for producing duplex stainless steel (DSS) components. HIP consolidates metal powders or preforms under high temperature and pressure, resulting in fully dense materials with improved mechanical properties and reduced porosity [7–9]. However, due to the high alloy content of SAF2507, microstructural changes can occur during the HIP process, including the formation of carbides, nitrides, secondary

Check for updates

Academic Editors: Belén Díaz Fernández and Eric Hug

Received: 28 April 2026
Revised: 4 June 2026
Accepted: 5 June 2026
Published: 10 June 2026

Copyright: © 2026 by the authors. Licensee MDPI, Basel, Switzerland. This article is an open access article distributed under the terms and conditions of the Creative Commons Attribution (CC BY) license.

austenite (γ′), and intermetallic phases such as sigma (σ), chi (χ), and R phases. These secondary phases significantly affect the microstructure, mechanical properties, and especially the corrosion resistance of SAF2507 [10,11]. For instance, David et al. [12] demonstrated that increasing σ phase content leads to a decline in corrosion resistance, while Ramirez et al. [13] reported that the presence of secondary austenite is associated with inferior corrosion performance. Therefore, the elimination or mitigation of these detrimental phases is essential for accurately assessing and improving the corrosion behavior of DSS.

Post-HIP heat treatment, particularly solution treatment, plays a key role in refining the microstructure by dissolving harmful secondary phases, promoting a more uniform distribution of alloying elements, and restoring the optimal ferrite-austenite phase balance [14–16]. While conventional DSSs have been widely studied, there is limited research on how solution treatment affects the corrosion behavior of HIP-SAF2507.

This study investigates the effects of solution treatment on the microstructural evolution and corrosion resistance of HIP-SAF2507 duplex stainless steel. Microstructural characterization was carried out using scanning electron microscopy (SEM) and energy-dispersive X-ray spectroscopy (EDS), and corrosion behavior was evaluated through potentiodynamic polarization testing in chloride-containing environments. The results provide valuable insights for optimizing post-HIP thermal treatment strategies to enhance the corrosion resistance and service reliability of DSS components in aggressive environments.

2. Materials and Methods

2.1. Powder Preparation and Hot Isostatic Pressing

Gas-atomized SAF2507 super duplex stainless steel powder (Guanda New Material Technology Co., Ltd., Anshan, China) was encapsulated in a stainless steel capsule, evacuated to below 10 Pa, and sealed. The chemical composition of the stainless steel is shown in Table 1. The HIP process was carried out at 1200 °C under 150 MPa for 2 h, followed by furnace cooling. The consolidated billets were sectioned into blocks (10 × 10 × 20 mm^3) using wire electrical discharge machining for subsequent heat treatment and testing.

Table 1. Chemical composition of SAF2507 (wt%).

Alloy	Fe	Cr	Ni	Mo	Mn	C	N	Si	P	S
SAF2507	61.225	25.86	7.509	3.710	0.94	0.016	0.23	0.487	0.022	0.001

2.2. Solution Treatment

The HIP samples were subjected to solution treatment at 1080 °C for 1 h in a KSL-1700X muffle furnace (Hefei Kejing Materials Technology Co., Ltd., Hefei, China), followed by immediate water quenching to room temperature (23 ± 2 °C). The heat treatment parameters were selected based on the parameters reported in the following reference [16,17]. This heat treatment was aimed at dissolving potential deleterious secondary phases and restoring the optimal ferrite-austenite balance. Samples before and after solution treatment are referred to as HIP and HT, respectively.

2.3. Phase and Microstructural Characterization

X-ray diffraction (XRD) analysis was performed using an Ultima IV X-ray diffractometer (Shimadzu Corporation, Kyoto, Japan) with Cu Kα radiation (λ = 1.5406 Å), operated at 40 kV and 40 mA. Scans were conducted in the 2θ range of 30°~60° with a step size of 0.02°. Phase identification and semi-quantitative analysis were carried out using Jade 6 software.

Scanning electron microscopy was conducted on polished cross-sections using a Model JSM-6510La (JEOL Ltd., Tokyo, Japan) at 20 kV. Surface preparation involved grinding with

SiC papers up to 1200 grit, followed by polishing with 0.05 µm colloidal silica suspension. Elemental distributions and point analyses were obtained using an EDS system. Electron backscatter diffraction (EBSD) was performed on the same SEM platform equipped with an Oxford Symmetry EBSD detector (Oxford Instruments, Abingdon, UK). Analyses were carried out at 20 kV acceleration voltage with a step size of 0.3 µm and a working distance of ~15 mm. EBSD data were processed and analyzed using AztecCrystal2.1 software to determine grain orientation, phase distribution, and misorientation characteristics.

2.4. Electrochemical Testing

Electrochemical experiments were conducted at room temperature using a CHI 600E workstation (CH Instruments, Austin, TX, USA) in a conventional three-electrode cell. The sample served as the working electrode with an exposed area of 1 cm^2; a platinum sheet was used as the counter electrode, and an Ag/AgCl electrode (saturated KCl) was used as the reference. Prior to testing, samples were ground to 1200 grit, ultrasonically cleaned in ethanol, rinsed with deionized water, and dried under nitrogen. Detailed information on the working electrodes is shown in Table 2.

Table 2. Detailed information on electrochemical samples.

Sample	Process	Number of Samples	Number of Tests
HIP	Hot isostatic pressing	1	3
HT	Hot isostatic pressing + solution treatment	1	3

Open-circuit potential (OCP) was monitored for 1 h to ensure stability. Electrochemical impedance spectroscopy (EIS) was performed at OCP in the frequency range from 10^5 to 10^{-2} Hz using a sinusoidal AC amplitude of 10 mV. The resulting impedance spectra were fitted using the Zview2 software. Potentiodynamic polarization was then conducted from −0.8 to +1.3 V at a scan rate of 1 mV/s. All measurements were carried out in a static 3.5 wt% NaCl solution prepared from analytical-grade reagents and deionized water.

2.5. Surface Characterization After Corrosion

Post-electrochemical corroded surfaces were examined by SEM to analyze localized corrosion morphologies, including pit initiation and propagation features. Three-dimensional surface profiling was carried out using an OLYMPUS OLS5000 laser confocal microscope (Olympus Corporation, Tokyo, Japan) to evaluate pit geometry, including depth and volume. Data from multiple fields of view were averaged to ensure reproducibility.

2.6. X-Ray Photoelectron Spectroscopy (XPS)

To investigate the chemical composition of the passive film formed on the surface of steel, samples before and after solid solution treatment were immersed in a 3.5 wt% NaCl solution for 7 days to ensure the formation of a stable passive film on the surface. XPS analysis was performed using the Thermo Scientific ESCALAB 250Xi system (Thermo Fisher Scientific, Waltham, MA, USA), equipped with a monochromatic Al Kα X-ray source at an energy of 1486.6 eV. Survey and high-resolution spectra were collected for Fe 2p, Cr 2p and O 1s regions. Charge correction was performed using the C1s peak at 284.8 eV as a reference. Depth profiling was achieved via Ar^+ sputtering at 2 kV for successive 10 s intervals. Spectral deconvolution and quantitative analysis were performed using Advantage (6.9) software.

3. Results and Discussion

Figure 1 shows the XRD patterns of SAF2507 duplex stainless steel before and after solution treatment. The HIP sample exhibits a two-phase structure consisting predominantly of ferrite (α) and austenite (γ), along with weak diffraction peaks attributed to secondary intermetallic phases (σ phases). After solution treatment at 1080 °C for 1 h, these secondary phase peaks disappear, indicating effective dissolution during thermal exposure. This confirms that the applied heat treatment successfully homogenizes the microstructure by eliminating detrimental precipitates, in agreement with previous findings on super duplex stainless steels subjected to solution annealing [6]. Furthermore, a noticeable rightward shift in the main diffraction peaks is observed in the HT sample compared to the HIP condition. This shift suggests a change in the lattice parameter, commonly associated with a variation in phase composition. The increased intensity of α peaks relative to γ reflections indicates a phase balance shift toward higher ferrite content, while austenite peaks exhibit decreased intensity, suggesting partial dissolution or transformation of the γ phase during heat treatment. Such ferrite enrichment may result from chromium and molybdenum diffusion during solution treatment, stabilizing the ferritic phase at elevated temperature [18,19].

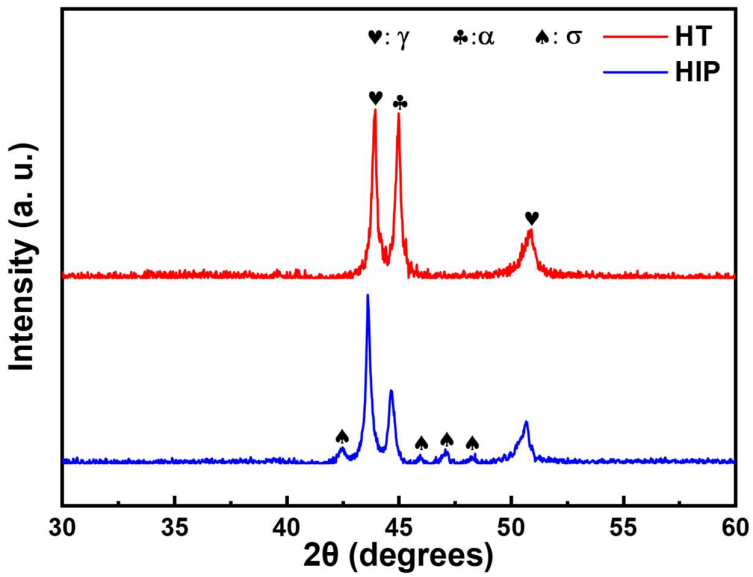


Figure 1. XRD patterns of SAF2507 specimens before and after solution treatment.

Figure 2 presents the backscattered electron (BSE) images and corresponding EDS elemental mapping of SAF2507 alloy in the HIP (Figure 2a) and HT (Figure 2b) conditions. Significant microstructural changes are observed after solution treatment. In the HIP condition (Figure 2a), the microstructure is characterized by a dual-phase morphology with γ islands distributed along the boundaries of polygonal α grains. Notably, secondary precipitates are visible at the α/γ interfaces and triple junctions. These are commonly identified in duplex stainless steels as intermetallic phases (σ phase), consistent with the XRD results shown in Figure 1. The distribution of alloying elements in the EDS maps supports this interpretation: Cr and Mo are enriched in σ phase regions. Additionally, the Ni map reveals higher intensity in the austenite phase, which is known to stabilize γ, while the ferrite grains exhibit elevated Cr and Mo levels. Table 3 presents the detailed EDS point scan data.

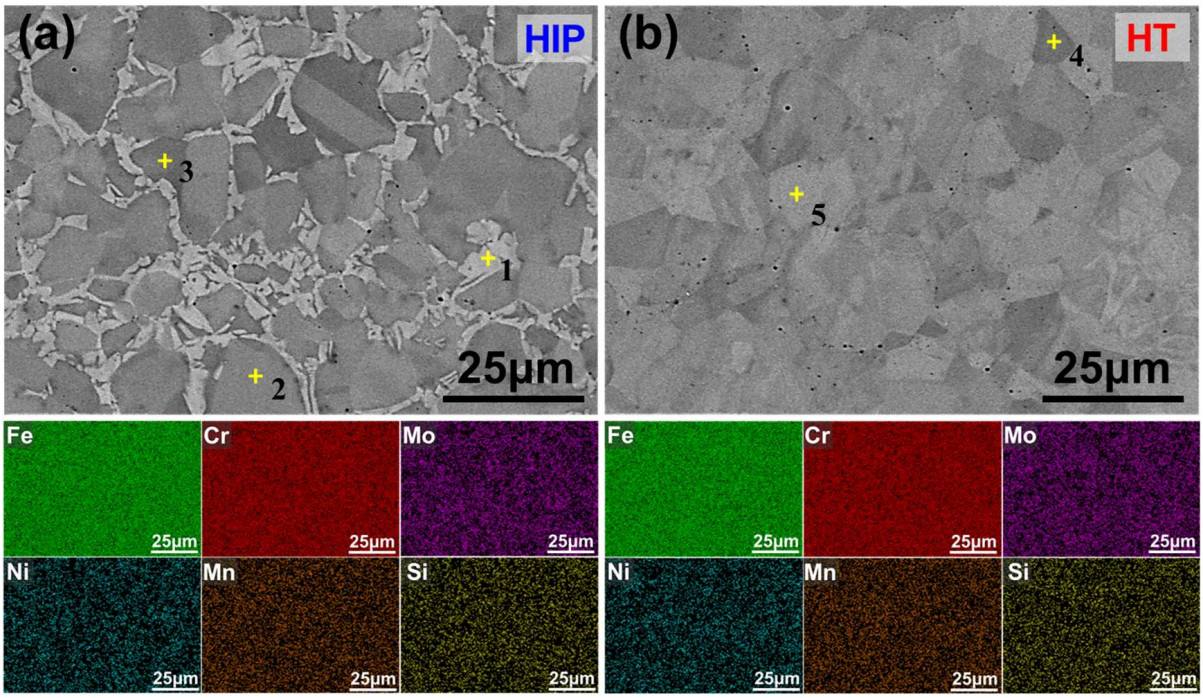


Figure 2. SEM micrographs and corresponding EDS elemental mappings of SAF2507 in the HIP and HT conditions. (**a**) HIP, (**b**) HT.

Table 3. Chemical composition (wt%) corresponding to each point in Figure 2.

Piont	Fe	Cr	Mo	Ni	Mn	Si	N
1	56.68	29.51	7.65	4.85	0.67	0.40	0.24
2	62.34	24.35	3.22	8.66	0.55	0.35	0.53
3	60.41	27.94	5.38	5.23	0.70	0.33	0.00
4	61.31	25.01	2.64	8.56	1.71	0.36	0.42
5	59.61	28.40	4.67	5.44	1.28	0.36	0.24

After solution treatment at 1080 °C for 1 h (Figure 2b), the microstructure becomes significantly more homogeneous. The precipitates previously observed at grain boundaries and triple junctions disappear, indicating their complete dissolution during solution annealing. The grain boundaries appear clean and free of secondary phases, suggesting improved microstructural stability. Overall, the solution treatment not only eliminates deleterious secondary phases but also promotes a more stable and chemically uniform duplex microstructure.

Electron backscatter diffraction was used to further evaluate the phase distribution, grain orientation, and texture characteristics of SAF2507 before and after solution treatment. Figure 3 displays the inverse pole figure (IPF) maps, phase maps, and grain size distributions of the HIP and HT samples. As shown in Figure 3a–c, the HIP sample presents a typical dual-phase microstructure composed of ferrite (α, blue) and austenite (γ/γ_2, red), with a significant number of fine precipitates identified as sigma phase (σ, green), primarily located at the α/γ interfaces and triple junctions. The presence of this intermetallic phase is consistent with both XRD (Figure 1) and SEM-EDS (Figure 2) results. The grain structure is relatively fine, with an average grain size of around 10 μm and a high frequency of small grains, as shown by the grain size distribution histogram (Figure 3c). This is attributed to the thermal and pressure conditions of HIP, which promote rapid nucleation and suppress grain growth. After solution treatment (Figure 3d–f), the sigma phase is almost completely eliminated, and the microstructure becomes cleaner and more homogeneous. The volume

fraction of ferrite increases, while austenite content decreases, suggesting a partial transformation of γ into α during thermal exposure. This is quantitatively confirmed by the phase fraction analysis in Figure 3g: the ferrite fraction increases from 26.93% to 46.60%, while austenite drops from 63.61% to 53.40%, and sigma phase is reduced from 9.46% to nearly undetectable levels. These changes are also consistent with the XRD peak intensity shifts discussed previously. In terms of crystallographic orientation, both conditions exhibit a relatively random texture, as indicated by the IPF triangle inset. No strong preferential orientation is observed, suggesting the absence of significant deformation-induced texture.

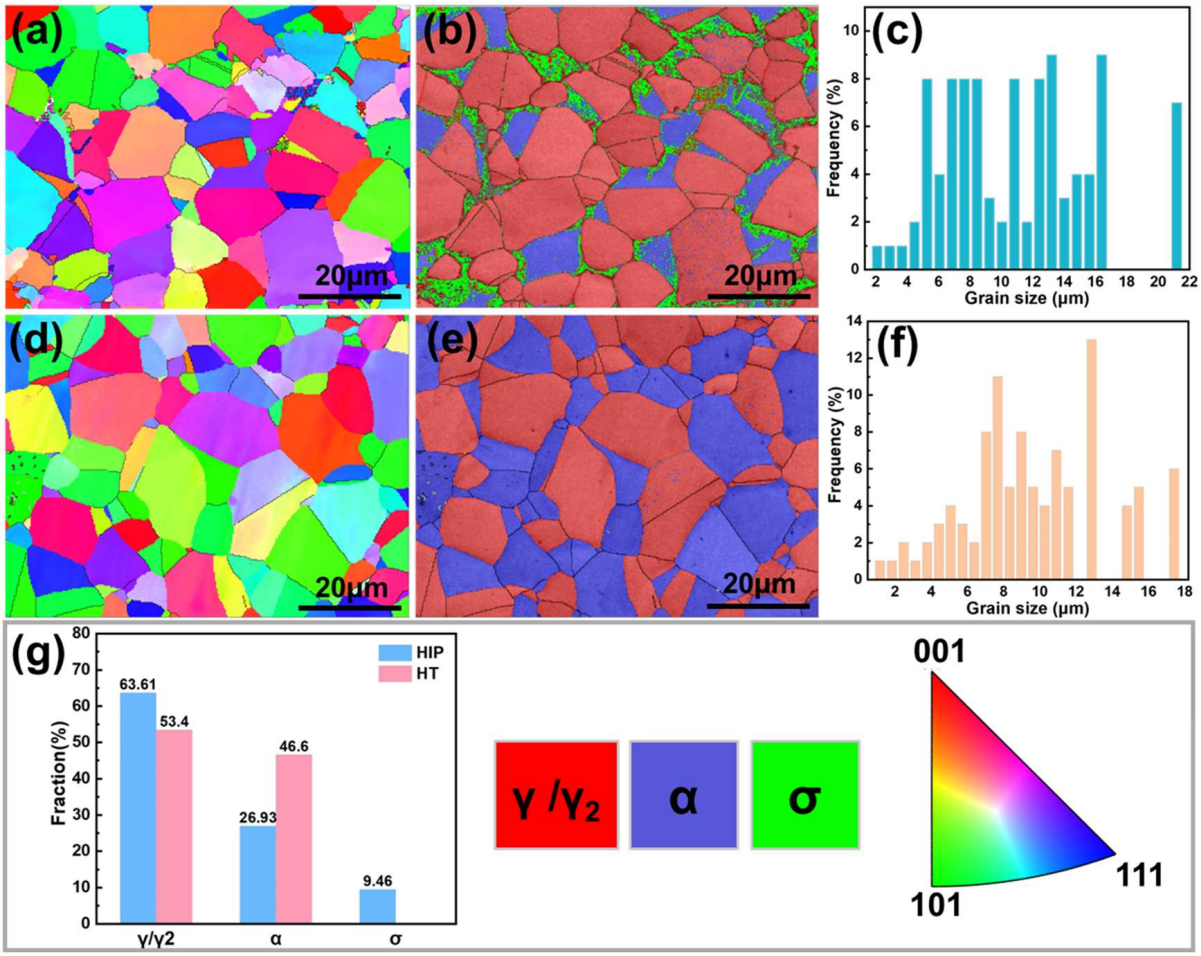


Figure 3. EBSD results of SAF2507 before and after solution treatment: (**a**,**d**) IPF maps, (**b**,**e**) phase maps, (**c**,**f**) average grain size distribution, and (**g**) phase fraction analysis.

Figure 4a presents the polarization curves of SAF2507 samples before and after solution treatment in 3.5 wt.% NaCl solution at room temperature. The corresponding electrochemical parameters are summarized in Table 4. The results reveal that neither the HIP nor the HT samples exhibit a distinct active-passive transition, suggesting that both are capable of spontaneously forming a passive film. Evidence of metastable pitting further indicates the breakdown and subsequent repair of the passive layer. Compared with the HIP condition, the solution-treated sample exhibits a broader passive region, a slightly lower corrosion current density (I_{corr}), and a higher pitting potential, indicating an improvement in corrosion resistance after solution treatment.

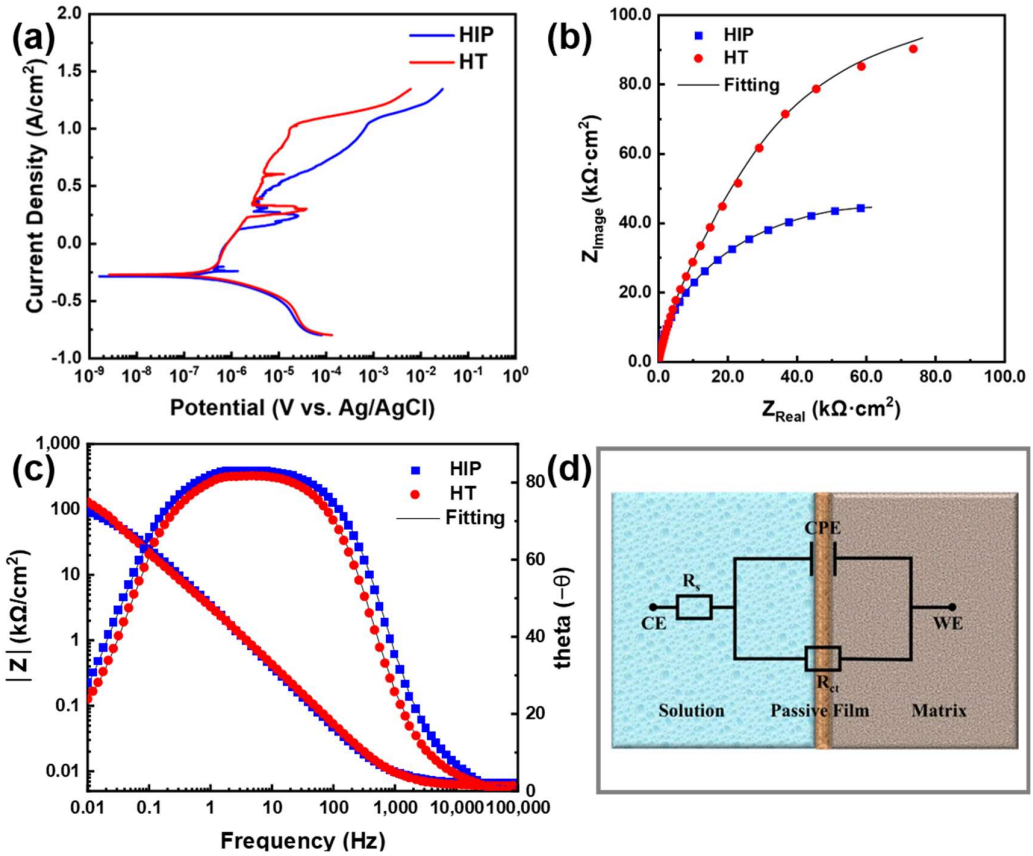


Figure 4. (**a**) Potentiodynamic polarization curves, (**b**) Nyquist plots, (**c**) Bode plots, and (**d**) Equivalent electrical circuit of SAF2507 before and after solution treatment in 3.5 wt% NaCl solution.

Table 4. Electrochemical parameters in the 3.5 wt% NaCl solution from potentiodynamic polarization curves.

Sample	E_{corr}/V	I_{corr}/A/cm^2	E_{pit}/V
HIP	-0.288 ± 0.023	$(4.504 \pm 0.114) \times 10^{-7}$	0.571 ± 0.013
HT	-0.272 ± 0.031	$(4.029 \pm 0.121) \times 10^{-7}$	1.008 ± 0.015

Figure 4b,c show the Nyquist and Bode plots for both samples under OCP. The order of the capacitive arc radius in the Nyquist plot is as follows: HT > HIP. This indicates that after solution treatment, the charge transfer resistance of SAF2507 increases, leading to improved corrosion resistance, which is consistent with the results from the polarization curves. According to the corresponding Bode plot, the impedance modulus decreases with increasing frequency in the low-frequency range. When the frequency range is 10–10^2 Hz, the phase angle reaches its maximum (~79°), indicating that surface inhomogeneity leads to non-ideal capacitive behavior [20]. Furthermore, the impedance modulus tends toward a wide plateau within the frequency range of 10–10^5 Hz. Feng et al. [21] suggested that the wide plateau in the impedance modulus is due to the pseudo-capacitive nature of the compact Cr-rich oxide layer. Therefore, a constant phase element (*CPE*) is used to replace the ideal pure capacitor. The protective performance of the passive film can be quantitatively analyzed by fitting the EIS data. Figure 4d presents the equivalent circuit model (EEC) used for fitting the EIS data, where R_s represents the solution resistance, and R_{ct} represents the charge transfer resistance at the solution/film interface. *CPE* is a constant phase element, representing the double-layer capacitance. The equivalent circuit, composed of R_s, R_{ct}, and *CPEs*, was selected to characterize the electrochemical response of the passive film and its non-ideal capacitive behavior [22]. The fitting parameters are

summarized in Table 5. During the EIS testing, due to the near-capacitive nature of the passive film, the electrochemical system essentially reflects the behavior of the solution resistance in the high-frequency region [23]. Therefore, the impedance modulus at 10^5 Hz for both samples is approximately 6 $\Omega \cdot cm^2$, with the corresponding phase angle being close to zero. Furthermore, R_{ct} is a key parameter for passivating alloys, and its value corresponds to the radius of the semicircle in the Nyquist plot, providing a good evaluation of the compactness and stability of the passive film formed on the alloy surface [24,25]. The results show that the HT samples exhibited the highest R_{ct} values, indicating that the corrosion rate of the solution-treated samples in the electrolyte was lower. This is attributed to the elimination of the σ-phase, which improved the integrity of the passivation film; the resulting difficulty in charge transfer between the passive film and the steel enhanced the protective capability of the passive film. These findings are consistent with the results reported in the literature [26]. *CPE* is used to quantitatively characterize the near-capacitive response of the alloy. The impedance of the *CPE* can be calculated using the following formula [27]:

$$Z_{CPE} = Q^{-1}(j\omega)^{-n} \quad (1)$$

where Q is the constant associated with the capacitance of the *CPE*; j is the imaginary unit; ω is the angular frequency; and n is the *CPE* exponent related to surface inhomogeneity. The chi-square (χ^2) values remain on the order of 10^{-3}, indicating a high precision of the EIS fit. From Table 5, it can be seen that the n values for the passive films of the two samples are 0.92 and 0.88, respectively. This deviation from the ideal capacitor value ($n = 1$) is attributed to surface roughness or other surface phenomena. In summary, both the polarization experiments and electrochemical impedance spectroscopy results indicate that the solution-treated sample exhibits superior corrosion resistance compared to the HIP sample.

Table 5. Parameters of the equivalent circuit diagram of the electrochemical impedance spectrum of the SAF2507 sample.

Sample	$R_s/\Omega \cdot cm^2$	$CPE/\Omega^{-1}\ cm^{-2}\ s^n$	n	$R_{ct}/\Omega \cdot cm^2$	χ_2
HIP	6.815 ± 0.513	(5.56 ± 0.24) × 10^{-5}	0.923 ± 0.01	92,767 ± 4000	(1.05 ± 0.24) × 10^{-3}
HT	6.042 ± 0.341	(6.37 ± 0.31) × 10^{-5}	0.884 ± 0.02	234,530 ± 6000	(1.12 ± 0.24) × 10^{-3}

Figure 5a,b show the corrosion morphologies of SAF2507 samples after polarization testing, in both the HIP and HT conditions, as observed by 3D laser confocal microscopy. The surface topography of the HIP sample (Figure 5a) reveals significant localized corrosion, with distinct pit formation and deep, sharp pits. These features suggest a relatively poor stability of the passive film under corrosion conditions. The height profile of the HIP sample (Figure 5b) shows large fluctuations, reflecting the pronounced depth and wide distribution of the pits. In contrast, the surface of the HT sample (Figure 5a_1) exhibits much less pronounced pitting corrosion. The overall surface appears smoother, with fewer and smaller pits, indicating improved passivation behavior after solution treatment. The corresponding height profile of the HT sample (Figure 5b_1) shows significantly reduced surface roughness (RSa, RSq) compared to the HIP sample. The smaller fluctuations in the height profile suggest that the passive film on the solution-treated sample is more stable, providing better protection against localized corrosion. This result is consistent with the electrochemical data (Figure 4), where the HT sample shows a lower corrosion current density and a more extensive passive region in the polarization curve. This indicates that solution treatment enhances the formation and stability of the passive film, significantly improving the corrosion resistance of SAF2507 in chloride-containing environments.

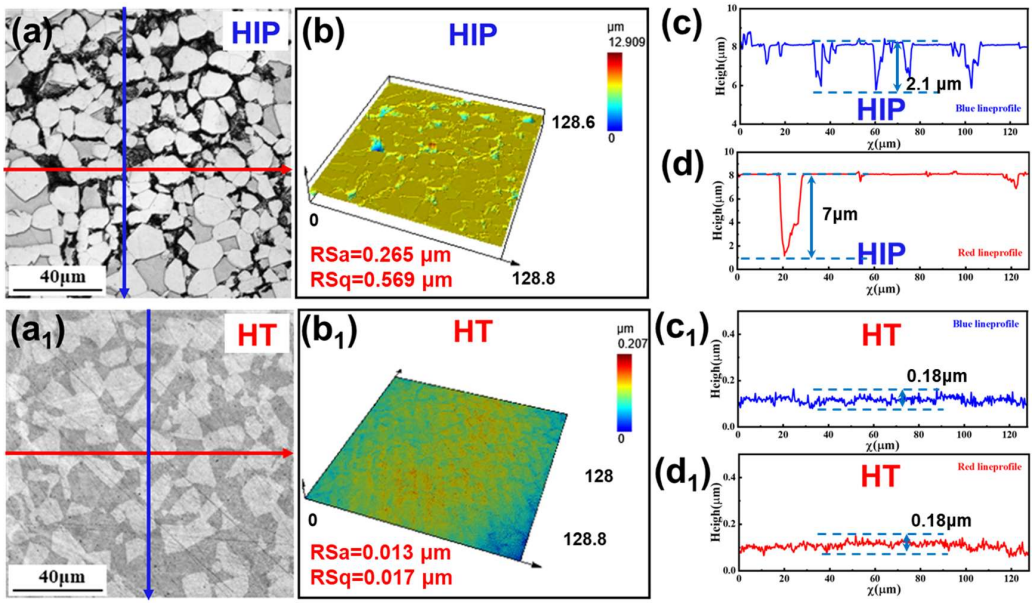


Figure 5. LSCM 2D, 3D and corresponding surface height profile images of the two states SAF2507: (**a**,**a**$_1$) 2D images, (**b**,**b**$_1$) 3D images, and (**c**,**c**$_1$,**d**,**d**$_1$) surface height profile images.

Figure 6 presents the corrosion morphologies of SAF2507 duplex stainless steel specimens before and after solution treatment following polarization testing. In chloride-containing environments, the corrosion process mainly involves anodic metal dissolution ($Fe \rightarrow Fe^{2+} + 2e^-$) and cathodic oxygen reduction ($O_2 + 2H_2O + 4e^- \rightarrow 4OH^-$). As shown, the HIP specimen exhibits numerous corrosion pits propagating along grain boundaries and phase interfaces. Corrosion primarily occurs in regions containing the σ phase, characterized by selective attack along σ-phase boundaries. According to the literature [28,29], during σ-phase precipitation, significant amounts of Cr and Mo are incorporated into the σ phase, resulting in local depletion of these essential alloying elements in adjacent areas, thereby creating corrosion-prone zones and reducing passive film stability. Therefore, passive film breakdown and localized charge transfer processes are considered the dominant rate-determining factors for corrosion propagation. In contrast, the surface of the solution-treated specimen appears smoother and shows significantly fewer corrosion features, indicating the formation of a more stable and compact passive film that effectively suppresses further corrosion. The dominant corrosion mode in the solution-treated sample is pitting. Line-scan EDS analysis in Figure 6d further reveals that the initiation of pitting corrosion is closely associated with the presence of Mo- and Mn-rich sulfide inclusions. These inclusions are susceptible to preferential dissolution in chloride-containing environments, leading to localized passive film breakdown and subsequent pit initiation [30,31].

Figure 7 presents the composition of the passive film on SAF2507 samples in two conditions after immersion in 3.5 wt% NaCl solution for 7 days. As shown in Figure 7a,d, the Cr $2p_{3/2}$ XPS spectra were deconvoluted into three peaks corresponding to Cr^0 (573 ± 0.2 eV), Cr_2O_3 (576 ± 0.2 eV), and $Cr(OH)_3$ (577 ± 0.2 eV). These results are consistent with previous reports in the literature [32]. It is well known that Cr_2O_3 is a key component of the passive film [33]. The Fe $2p_{3/2}$ spectra were fitted with four peaks, corresponding to Fe^0, Fe^{3+}_{ox}, Fe^{3+}_{hy}, and FeOOH, located at 706 ± 0.2 eV, 707 ± 0.2 eV, 709 ± 0.2 eV, and 711.5 ± 0.2 eV, respectively (Figure 7b,e) [22]. Figure 7c,f display the deconvoluted O 1s spectra of the two samples. Three peaks were identified at binding energies of 529.7 ± 0.2 eV, 531.4 ± 0.2 eV, and 528.9 ± 0.2 eV, corresponding to O^{2-}, OH^-, and H_2O, respectively [34]. The presence of O^{2-} and OH^- indicates the formation of metal oxides and hydroxides on the alloy surface [35,36].

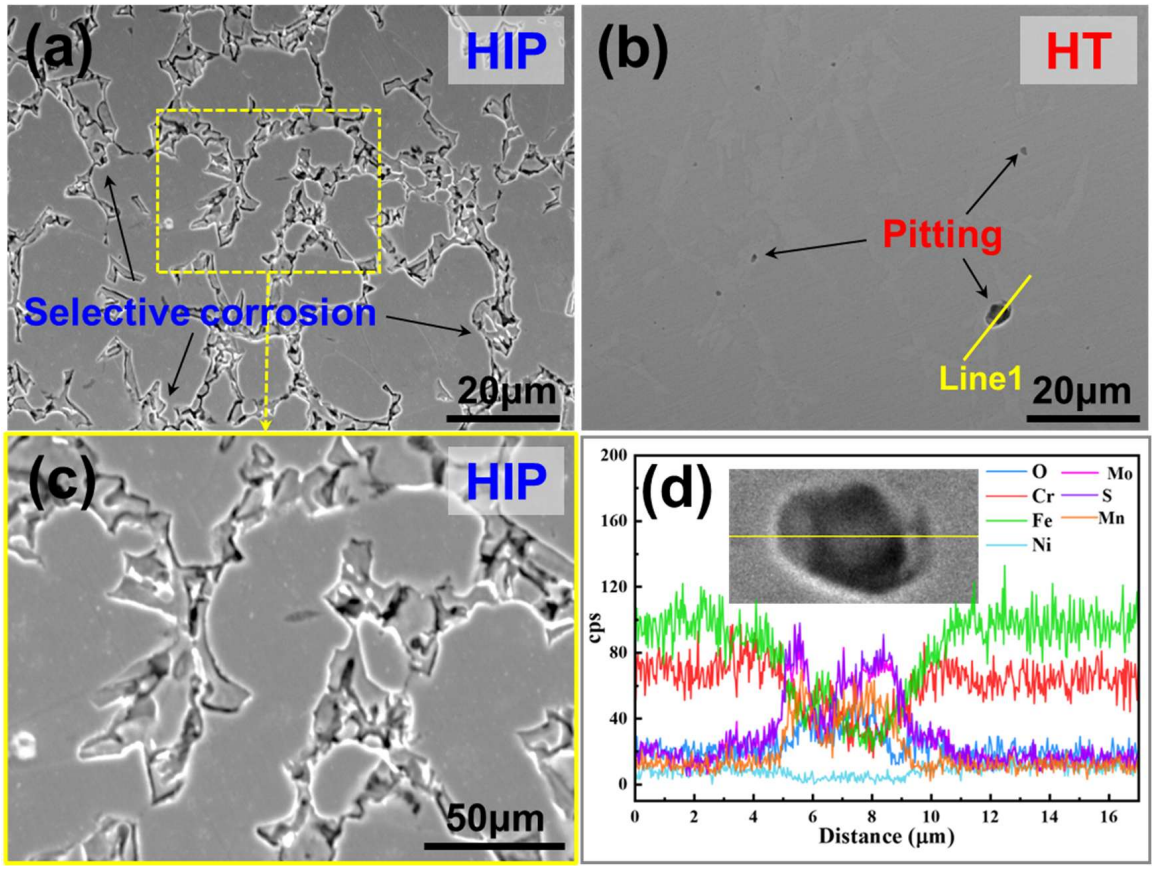


Figure 6. Microscopic morphology of HIP (**a**,**c**) and HT (**b**) samples after polarization testing; (**d**) line scan corresponding to (**b**) in the figure.

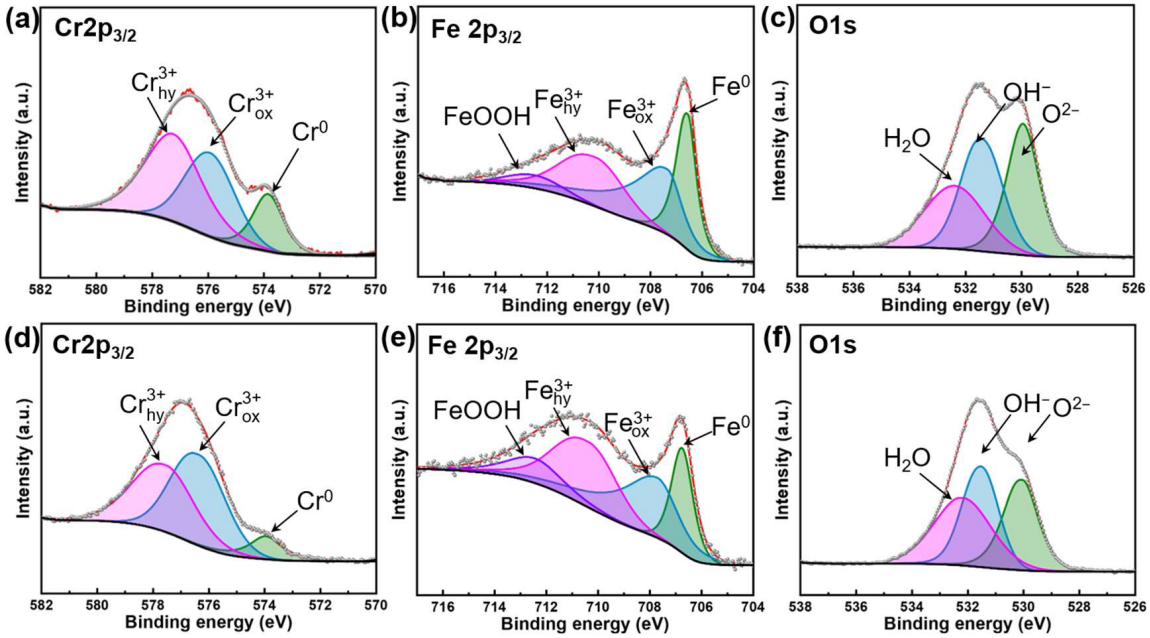


Figure 7. High-resolution XPS spectra of Cr 2p, Fe 2p and O 1s for SAF2507 before (**a**–**c**) and after (**d**–**f**) solution treatment after 7 days of immersion in 3.5 wt% NaCl solution at room temperature.

To further investigate the elemental composition of the passive films, the atomic percentages of the metallic elements in the passive layers of the two HEAs were calculated using the following equation [37]:

$$C_x = \frac{I_x / S_x}{\sum(I_i / S_i)} \quad (2)$$

where C_x is the atomic percentage of element in the passive films, I_x represents the peak intensity corresponding to each element, and S_x denotes the sensitivity factor obtained from the XPS instrument. Figure 8a illustrates the chemical states and corresponding cationic fractions of Fe, Cr, and O elements within the passive film of SAF2507 samples before and after solution treatment. The results indicate that it significantly influences stability and corrosion resistance [38,39]. Prior to solution treatment, Fe primarily exists in the form of Fe_2O_3 (47.41%) and Fe^{3+}_{hy} (20.28%), with a small amount of FeOOH (7.49%). Cr is predominantly present as $Cr(OH)_3$ (47.05%), while Cr_2O_3 accounts for only 35.26%. Additionally, the O element consists mainly of unstable species such as OH^- (34.40%) and H_2O (36.18%). In contrast, after solution treatment, the FeOOH content markedly increases to 25.23%, while the Fe^{3+}_{hy} fraction decreases to 28.73%. The Cr_2O_3 content rises to 50.37%, accompanied by a reduction in $Cr(OH)_3$ to 41.10%. Moreover, the proportion of O^{2-} increases from 29.41% to 34.86%, suggesting that solution treatment promotes the enrichment of more stable oxide species in the passive film, thereby enhancing its density and protective performance [39,40]. To further quantify the stability of the passive film, Figure 8b presents a comparative analysis of the Cr_{ox}/Cr_{hy}, O_{ox}/O_{hy}, and $(Cr_{ox+hy})/(Fe_{ox+hy})$ ratios. The results show that the Cr_{ox}/Cr_{hy} and O_{ox}/O_{hy} ratios increase after solution treatment, with a particularly significant rise in the total $(Cr_{ox+hy})/(Fe_{ox+hy})$ ratio. This indicates greater enrichment of chromium oxides and a relative reduction of iron oxides in the passive film, contributing to the formation of a denser and more stable passive layer. Consequently, the corrosion resistance of the material in chloride-containing environments is significantly improved [41,42].

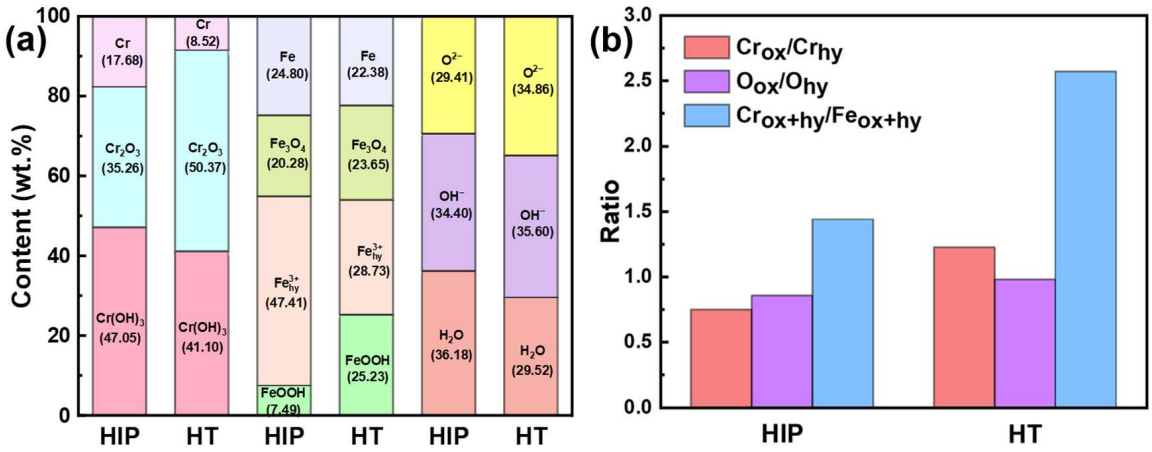


Figure 8. (**a**) Contents of various Fe, Cr, and O components and (**b**) ratios of Cr_{ox} to Cr_{hy}, O_{ox} to O_{hy}, and Cr_{ox+hy} to Fe_{ox+hy} in passive films on surfaces of SAF2507 before and after solution treatment after 7 days of immersion in 3.5 wt% NaCl solution at room temperature.

4. Conclusions

This study demonstrates that solution treatment significantly improves the microstructural uniformity and corrosion resistance of SAF2507 duplex stainless steel fabricated by direct hot isostatic pressing. The main conclusions are as follows:

(1) Solution treatment at 1080 °C for 1 h effectively dissolves intermetallic phases and promotes a homogeneous distribution of ferrite and austenite.
(2) The solution-treated alloy exhibits a slightly lower corrosion current density, together with a wider passive region, higher pitting potential, and improved charge transfer resistance in 3.5 wt.% NaCl solution, indicating enhanced resistance to localized corrosion and improved passive film stability.
(3) EIS analysis shows that the treated sample has higher charge transfer resistance, suggesting the formation of a denser and more protective passive film.
(4) XPS results reveal an increased proportion of Cr_2O_3 and O^{2-} and a decrease in Fe_2O_3 and H_2O in the passive layer, confirming improved film stability.
(5) Surface and corrosion morphology analyses confirm that solution treatment suppresses selective corrosion and pitting, enhancing the uniformity and protectiveness of the passive film.

Author Contributions: Conceptualization, D.J. and L.C.; methodology, P.Z., J.L. and B.W.; software, B.W. and Z.W.; validation, D.J., L.C. and Z.W.; formal analysis, B.W. and J.L.; investigation, P.Z.; resources, Z.W.; data curation, B.W. and P.Z.; writing-original draft preparation, J.L. and B.W.; writing—review and editing, D.J.; visualization, Z.W.; supervision, L.C.; project administration, D.J.; P.Z. and L.C. All authors have read and agreed to the published version of the manuscript.

Funding: This research received no external funding.

Data Availability Statement: The data presented in this study are available on request from the corresponding author.

Conflicts of Interest: Authors Zhanfang Wu, Pengjie Zhang and Lida Che were employed by the company CISRI HIPEX Technology CO., LTD, Beijing, China. The remaining authors declare that the research was conducted in the absence of any commercial or financial relationships that could be construed as a potential conflict of interest.

References

1. Salvetr, P.; Školáková, A.; Melzer, D.; Brázda, M.; Duchoň, J.; Drahokoupil, J.; Svora, P.; Msallamová, Š.; Novák, P. Characterization of super duplex stainless steel SAF2507 deposited by directed energy deposition. *Mater. Sci. Eng. A* **2022**, *857*, 144084. [CrossRef]
2. Haghdadi, N.; Ledermueller, C.; Chen, H.; Chen, Z.; Liu, Q.; Li, X.; Rohrer, G.; Liao, X.; Ringer, S.; Primig, S. Evolution of microstructure and mechanical properties in 2205 duplex stainless steels during additive manufacturing and heat treatment. *Mater. Sci. Eng. A* **2022**, *835*, 142695. [CrossRef]
3. Gunn, R. *Duplex Stainless Steels: Microstructure, Properties and Applications*; Woodhead Publishing: Sawston, UK, 1997.
4. Zhang, Z.; Zhang, H.; Zhao, H.; Li, J. Effect of prolonged thermal cycles on the pitting corrosion resistance of a newly developed LDX 2404 lean duplex stainless steel. *Corros. Sci.* **2016**, *103*, 189–195. [CrossRef]
5. Zhang, X.; Wang, K.; Zhou, Q.; Ding, J.; Ganguly, S.; Marzio, G.; Yang, D.; Xu, X.; Dirisu, P.; Williams, S.W. Microstructure and mechanical properties of TOP-TIG-wire and arc additive manufactured super duplex stainless steel (ER2594). *Mater. Sci. Eng. A* **2019**, *762*, 138097. [CrossRef]
6. Zhang, Z.; Zhang, H.; Hu, J.; Qi, X.; Bian, Y.; Shen, A.; Xu, P.; Zhao, Y. Microstructure evolution and mechanical properties of briefly heat-treated SAF 2507 super duplex stainless steel welds. *Constr. Build. Mater.* **2018**, *168*, 338–345. [CrossRef]
7. Liu, Z.; Tan, Z.; He, D.; Zhou, Z.; Guo, X.; Shao, W.; Yao, H.; Xue, Y.; Cui, L. Simultaneously improved the strength and ductility of laser powder bed fused Al-Cr-Fe-Ni-V high-entropy alloy by hot isostatic pressing: Microcrack closure and precipitation strengthening. *J. Mater. Sci. Technol.* **2024**, *180*, 55–68. [CrossRef]
8. Joseph, J.; Hodgson, P.; Jarvis, T.; Wu, X.; Stanford, N.; Fabijanic, D.M. Effect of hot isostatic pressing on the microstructure and mechanical properties of additive manufactured AlxCoCrFeNi high entropy alloys. *Mater. Sci. Eng. A* **2018**, *733*, 59–70. [CrossRef]
9. Li, X.; Wang, Q.; Wei, S.; Lou, W.; Liang, J.; Chen, L.; Xu, L.; Zhou, Y. Microstructure and high-temperature mechanical properties of Cu-W composite prepared by hot isostatic pressing. *J. Alloy. Compd.* **2024**, *970*, 172571. [CrossRef]
10. Nilsson, J.-O. Technology, Super duplex stainless steels. *Mater. Sci.* **1992**, *8*, 685–700.
11. Angelini, E.; De Benedetti, B.; Rosalbino, F. Microstructural evolution and localized corrosion resistance of an aged superduplex stainless steel. *Corros. Sci.* **2004**, *46*, 1351–1367. [CrossRef]

12. Silva, D.D.; Lima, L.S.; Araújo, A.J.; Silva, V.D.; Raimundo, R.A.; Damasceno, I.Z.; Simões, T.A.; Gomes, R.M. The Effect of Microstructural Changes on Mechanical and Electrochemical Corrosion Properties of Duplex Stainless Steel Aged for Short Periods. *Materials* **2020**, *13*, 5511–5524. [CrossRef]
13. Ramirez, A.J.; Lippold, J.C.; Brandi, S.D. The relationship between chromium nitride and secondary austenite precipitation in duplex stainless steels. *Met. Mater. Trans. A* **2003**, *34*, 1575–1597. [CrossRef]
14. Chen, T.; Yang, J. Effects of solution treatment and continuous cooling on σ-phase precipitation in a 2205 duplex stainless steel. *Mater. Sci. Eng. A* **2001**, *311*, 28–41. [CrossRef]
15. Hwang, H.; Park, Y. Effects of heat treatment on the phase ratio and corrosion resistance of duplex stainless steel. *Mater. Trans.* **2009**, *50*, 1548–1552. [CrossRef]
16. Ren, X.; Li, S.; Xiong, Z. Isostatic diffusion bonding and post-solution treatment between Cr22Ni5Mo3MnSi and Cr30Ni7Mo3MnSi duplex stainless steels. *J. Manuf. Process.* **2018**, *34*, 215–224. [CrossRef]
17. Li, S.; Wang, Y.; Zhang, H.; Li, S.; Wang, G.; Wang, X. Effects of prior solution treatment on thermal aging behavior of duplex stainless steels. *J. Nucl. Mater.* **2013**, *441*, 337–342. [CrossRef]
18. Tütük, I.; Ural, M.M.; Özer, G.; Kisasöz, A. Influence of solution treatment process on the properties of duplex stainless steels: A comparative study on microstructure and corrosion properties of UNS S32205 and UNS S32760. *Met. Mater. Trans. B* **2024**, *55*, 2916–2921. [CrossRef]
19. Li, J.; Shen, W.; Lin, P.; Wang, F.; Yang, Z. Effect of solution treatment temperature on microstructural evolution, precipitation behavior, and comprehensive properties in UNS S32750 super duplex stainless steel. *Metals* **2020**, *10*, 1481. [CrossRef]
20. Allahkaram, S.; Nazari, M.H.; Mamaghani, S.; Zarebidaki, A. Characterization and corrosion behavior of electroless Ni–P/nano-SiC coating inside the CO2 containing media in the presence of acetic acid. *Mater. Des.* **2011**, *32*, 750–755. [CrossRef]
21. Feng, L.; Yang, Y.; Zhao, Y.; Ma, K.; Cui, J. Corrosion behaviors and mechanism of AlxCrFeMnCu high-entropy alloys in a 3.5 wt% NaCl solution. *Corros. Sci.* **2024**, *233*, 112087. [CrossRef]
22. Xu, Z.; Zhang, H.; Du, X.; He, Y.; Luo, H.; Song, G.; Mao, L.; Zhou, T.; Wang, L. Corrosion resistance enhancement of CoCrFeMnNi high-entropy alloy fabricated by additive manufacturing. *Corros. Sci.* **2020**, *177*, 108954. [CrossRef]
23. Zhang, J.; Zhou, Y.; Ren, Z.; Luan, J.; Zhao, Y.; Yang, T. The influence of microstructural evolutions on electrochemical corrosion and passive behavior in precipitation-strengthened high-entropy alloys. *Corros. Sci.* **2024**, *233*, 112074. [CrossRef]
24. Hong, M.-S.; Kim, S.-H.; Im, S.-Y.; Kim, J.-G. Effect of ascorbic acid on the pitting resistance of 316L stainless steel in synthetic tap water. *Met. Mater. Int.* **2016**, *22*, 621–629. [CrossRef]
25. Zhong, J.-Y.; Sun, M.; Liu, D.-B.; Li, X.-G.; Liu, T.-Q. Effects of chromium on the corrosion and electrochemical behaviors of ultra high strength steels. *Int. J. Miner. Met. Mater.* **2010**, *17*, 282–289. [CrossRef]
26. Liu, H.; Jiang, B.; Du, X.; Zheng, X.; Wang, Z.; Yang, H.; Xu, T.; Xiao, A.; Pan, Y.; Yang, W.; et al. The effect of sigma phase of 2507 duplex stainless steel on hydrogen-induced pitting corrosion. *Corros. Sci.* **2026**, *260*, 113594. [CrossRef]
27. Zhao, Q.; Pan, Z.; Wang, X.; Luo, H.; Liu, Y.; Li, X. Corrosion and passive behavior of AlxCrFeNi3−x (x = 0.6, 0.8, 1.0) eutectic high entropy alloys in chloride environment. *Corros. Sci.* **2022**, *208*, 110666. [CrossRef]
28. Adhe, K.M.; Kain, V.; Madangopal, K.; Gadiyar, H.S. Influence of sigma-phase formation on the localized corrosion behavior of a duplex stainless steel. *J. Mater. Eng. Perform.* **1996**, *5*, 500–506. [CrossRef]
29. Hosseini, V.A.; Karlsson, L.; Wessman, S.; Fuertes, N. Effect of sigma phase morphology on the degradation of properties in a super duplex stainless steel. *Materials* **2018**, *11*, 933. [CrossRef] [PubMed]
30. Chiba, A.; Muto, I.; Sugawara, Y.; Hara, N. Pit initiation mechanism at MnS inclusions in stainless steel: Synergistic effect of elemental sulfur and chloride ions. *J. Electrochem. Soc.* **2013**, *160*, C511–C520. [CrossRef]
31. Li, D.; Huang, F.; Lei, X.; Jin, Y. Localized corrosion of 304 stainless steel triggered by embedded MnS. *Corros. Sci.* **2023**, *211*, 110860. [CrossRef]
32. Zhu, M.; He, F.; Yuan, Y.F.; Yin, S.M.; Guo, S.Y.; Pan, J. Effect of aging time on the microstructure and corrosion behavior of 2507 super duplex stainless steel in simulated marine environment. *J. Mater. Eng. Perform.* **2021**, *30*, 5652–5666. [CrossRef]
33. Gao, W.-B.; Gu, Y.; Han, Q.-L.; Gu, X.-Y.; Guan, W.; Zhao, S.-B.; Li, W.-H. Corrosion and passivation behavior of sensitized SAF 2507 super-duplex stainless steel in hot concentrated seawater. *J. Iron Steel Res. Int.* **2025**, *32*, 3026–3045. [CrossRef]
34. Liu, J.; Yang, S.; Huang, Y.; Yang, H.; Ju, D.; Che, L.; Li, X.; Wu, Z. Effects of nitric acid passivation on the corrosion resistance of CoCrFeMnNi high-entropy alloy prepared by hot isostatic pressing. *Mater. Chem. Phys.* **2025**, *345*, 131208. [CrossRef]
35. Liu, J.; Ju, D.; Zhang, J.; Cheng, Y.; Wu, Z.; Che, L.; Li, X.; Lv, Z. Enhance corrosion resistance via passivation treatment for CrMnFeCoNi high-entropy alloy prepared by hot isostatic pressing. *Intermetallics* **2025**, *184*, 108846. [CrossRef]
36. Davenport, A.J.; Oblonsky, L.J.; Ryan, M.P.; Toney, M.F. The structure of the passive film that forms on iron in aqueous environments. *J. Electrochem. Soc.* **2000**, *147*, 2162–2173. [CrossRef]
37. Liu, J.; Cheng, Y.; Zhang, J.; Chen, C.; Zheng, C.; Ju, D.; Wu, Z.; Che, L.; Li, X.; Lv, Z. Effect of phosphorus on the corrosion resistance of CrMnFeCoNi high-entropy alloys prepared by hot isostatic pressing. *J. Alloy. Compd.* **2025**, *1039*, 183157. [CrossRef]

38. Olsson, C.-O.; Landolt, D. Passive films on stainless steels—Chemistry, structure and growth. *Electrochim. Acta* **2003**, *48*, 1093–1104. [CrossRef]
39. Liu, M.; Cheng, X.; Li, X.; Pan, Y.; Li, J. Effect of Cr on the passive film formation mechanism of steel rebar in saturated calcium hydroxide solution. *Appl. Surf. Sci.* **2016**, *389*, 1182–1191. [CrossRef]
40. Carmezim, M.; Simões, A.; Figueiredo, M.; Belo, M.D.C. Electrochemical behaviour of thermally treated Cr-oxide films deposited on stainless steel. *Corros. Sci.* **2002**, *44*, 451–465. [CrossRef]
41. Sun, M.; Yang, Z.; Song, S.; Zhang, J.; Lu, B. Effect of Cr content on microstructure, mechanical, and corrosion properties of CoCr FeMnNi high-entropy alloys fabricated by selective laser melting. *Mater. Charact.* **2024**, *212*, 113949. [CrossRef]
42. Liu, J.; Lv, Z.; Wu, Z.; Zhang, J.; Zheng, C.; Chen, C.; Ju, D.; Che, L. Research progress on the influence of alloying elements on the corrosion resistance of high-entropy alloys. *J. Alloy. Compd.* **2024**, *1002*, 175394. [CrossRef]

Disclaimer/Publisher's Note: The statements, opinions and data contained in all publications are solely those of the individual author(s) and contributor(s) and not of MDPI and/or the editor(s). MDPI and/or the editor(s) disclaim responsibility for any injury to people or property resulting from any ideas, methods, instructions or products referred to in the content.